SIAM J. SCI. COMPUT.
Vol. 30, No. 3, pp. 1634–1657

ADAPTIVE FINITE ELEMENT METHOD FOR A PHASE FIELD BENDING ELASTICITY MODEL OF VESICLE MEMBRANE DEFORMATIONS*

QIANG DU† AND JIAN ZHANG†

Abstract. In this paper, a three-dimensional adaptive finite element method is developed for a variational phase field bending elasticity model of vesicle membrane deformations. Using a mixed finite element formulation, residual type a posteriori error estimates are derived for the associated nonlinear system of equations and, they are used to introduce the mesh refinement and coarsening. The resulting mesh adaptivity significantly improves the efficiency of the phase field simulation of vesicle membranes and enhances its capability in handling complex shape and topological changes. The effectiveness of the adaptive method is further demonstrated through numerical examples.

Key words. vesicle membrane, phase field, elastic bending energy, a posteriori error estimator, adaptive finite element, mixed finite element

AMS subject classifications. 65N30, 70G75, 92C05

DOI. 10.1137/060656449

1. Introduction.

This paper presents an adaptive finite element method for the numerical simulation of vesicle membrane deformation based on a phase field bending elasticity model. The vesicle membranes, formed by bilayers of lipid molecules, are simple forms of biological membranes which exist everywhere in life and compartmentalize living matter into cells and subcellular structures, and are essential for many biological functions [38]. The equilibrium shapes of bilayer vesicle membranes have been successfully modeled via the minimization of certain shape energy; see, for instance, [14, 36, 41, 48], and the references cited therein.

In the isotropic case, the most relevant energetic contribution to the equilibrium membrane geometry is usually the elastic bending energy of the form [11, 12, 41]:

$$E_{elastic} = \int_\Gamma \frac{k}{2} H^2 \, ds, \tag{1.1}$$

where H is the mean curvature of the membrane surface. The parameter k is the bending rigidity, which can depend on the local heterogeneous concentration of the species (such as protein and cholesterol molecules), but it is mostly assumed to be a constant in this manuscript. Taking a simplified description of the effect of density change and osmotic pressure, it is assumed that the variation of the bending energy is subject to the constraints of specified volume and surface area. More general forms of the bending elastic energy, attributed to Canham and Helfrich, also incorporate effects of surface tension, the Gaussian curvature, and the spontaneous curvature [36, 41]. For the sake of simplicity in our presentation, we only focus on the energy (1.1), though much of our studies can be naturally extended to more general cases including the effect of the spontaneous curvature [20], the Gaussian curvature [21, 24], and the vesicle fluid interactions [17, 18].

*Received by the editors April 5, 2006; accepted for publication (in revised form) October 31, 2007; published electronically April 18, 2008. This research is supported in part by NSF-DMR 0205232 and NSF-DMS 0712744.

http://www.siam.org/journals/sisc/30-3/65644.html

†Department of Mathematics, Pennsylvania State University, University Park, PA 16802 (qdu@math.psu.edu, zhang_j@math.psu.edu).

Computationally, there are many simulation methods developed for studying various deforming interface problems, such as the boundary integral and boundary element methods, immersed boundary and interface methods, front-tracking methods, and level-set methods (see, for instance, [34, 40, 43, 46, 49], and the references given in [22, 23]). For bending elasticity models, applications of these types of methods can also be found in [6, 28, 32, 53]. The phase field model can be viewed as a physically motivated level-set method; this is by virtue of its energy-based variational formalism. One of the main attractions to use the phase field method is its capability of easily incorporating the complex morphological changes of the interface, in particular, the changes in both topological and geometrical structures. For more detailed discussions, we refer to [22, 23], and the references given there.

In [22], a finite difference method was used to study the energy-minimizing vesicle membrane in the three-dimensional axis-symmetric case. In [23], a Fourier spectral method was used to study the full three-dimensional case. Parallel implementation of such a spectral approach was also carried out to improve the computational efficiency. The various simulation examples given in the earlier studies demonstrated the effectiveness of the phase field approach. However, in the three-dimensional case, the high computational cost remains a formidable challenge in making the phase field simulation efficient. Indeed, the phase field function is defined on the whole physical domain, and it changes rapidly only near the transition layer around the membrane surface (the zero level set of the phase field function). Hence, uniform computational grids are generally not optimal, and it is natural to consider the application of adaptive finite element methods based on a posteriori error estimators [2, 3, 50]. We anticipate that adaptivity based on effective error estimations could make the phase field simulation much more efficient computationally and yet retain the advantage of being able to avoid the explicit tracking of the interfaces. This is indeed confirmed by the present work.

In the adaptive method presented in this paper, a mixed finite element method (FEM) is used to discretize the phase field bending elasticity model. A residual-type a posteriori error estimator is derived for the development of the adaptive FEM algorithm. Effectively, the nodes of the adaptive mesh are concentrated near the interface (the membrane surface) so that the number of nodes is significantly reduced compared with the number of nodes in the uniform mesh cases, while the resolution of the numerical resolution of the adaptive FEM remains at the same level. These numerical results reveal the great potential of using the adaptive FEM to significantly reduce the computational cost of phase field approaches.

Detailed descriptions, analysis, and numerical examples of our adaptive FEM approach are presented in the rest of the paper as follows: in section 2, a brief introduction is given to the phase field bending elasticity model for the vesicle membrane problem. In section 3, we set up a finite element discretization for the model based on a mixed formulation. In section 4, we derive some a posteriori error estimators. In section 5, an adaptive algorithm is outlined along with discussions on other implementation issues involved. In section 6, numerical examples are presented, and finally, in section 7, some concluding remarks are given.

2. The phase field bending elasticity model. As in [22, 23], we introduce a phase function $\phi = \phi(x)$ defined on the physical (computational) domain Ω, which is used to label the inside and the outside of the vesicle Γ. The level set $\{x : \phi(x) = 0\}$ gives the membrane surface Γ, while $\{x : \phi(x) > 0\}$ represents the outside of the membrane and $\{x : \phi(x) < 0\}$ the inside. The original elastic bending energy model

consists of minimizing (1.1) among all surfaces with specified surface area and enclosed volume.

Define the following modified elastic energy:

$$E(\phi) = \int_\Omega \frac{k\epsilon}{2}\left(\triangle\phi - \frac{1}{\epsilon^2}(\phi^2-1)\phi\right)^2 dx, \tag{2.1}$$

where ϵ is a transition parameter which is taken to be very small compared to the size of the vesicle. In our numerical examples, ϵ varies in the same range of that in [23], that is, taking values generally about 1/40 to 1/200 of the size of Ω to ensure a sufficient level of resolution of the interface and the phase field solution profile.

For a minimizer ϕ of $E(\phi)$, it has been shown that

$$H(\phi) = \epsilon\left(\triangle\phi - \frac{1}{\epsilon^2}(\phi^2-1)\phi\right)$$

is the phase field approximation of the mean curvature H of the interface, which behaves like a measure concentrated in the diffuse interfacial layer of the zero level set of ϕ as ϵ goes to zero [23, 25]. Notice that the definition of $E(\phi)$ is

$$E(\phi) = \frac{1}{\epsilon}\int_\Omega \frac{k}{2}H^2(\phi)dx,$$

with the normalizing factor $1/\epsilon$ accounting for the contribution due to the diffuse interfacial layer. The phase field bending elasticity model is then given by minimizing the above energy $E(\phi)$ subject to prescribed values of

$$A(\phi) = \int_\Omega \phi(x)dx \quad \text{and} \quad B(\phi) = \int_\Omega \left[\frac{\epsilon}{2}|\nabla\phi|^2 + \frac{1}{4\epsilon}(\phi^2-1)^2\right]dx\,. \tag{2.2}$$

Intuitively, it is insightful to consider a special phase field function of the form $\phi(x) = \tanh(\frac{d(x,\Gamma)}{\sqrt{2}\epsilon})$, where $d(x,\Gamma)$ is the signed distance from a point $x \in \Omega$ to the surface Γ; the geometric meanings of the energy E and the constraints (2.2) would then become clear. More rigorously, the existence of the minimizer to $E(\phi)$ subject to prescribed $A(\phi)$ and $B(\phi)$ has been established in [25]. Moreover, it has been shown in [19, 51] that under some general ansatz assumptions, as $\epsilon \to 0$, the minimum of the phase field energy $E(\phi)$ with the specified constraints approaches to the minimum of the original energy (1.1), with $A(\phi)$ approaching the difference of the outside volume and the inside volume of the membrane surface and $B(\phi)$ approaching to $2\sqrt{2}/3$ times the surface area of Γ. The previously developed finite difference, finite element, and spectral methods in [22, 23, 25, 26] are based on the above phase field bending elasticity model. Some convergence analysis and a priori error estimates have been given in [25, 26].

3. The finite element discretization. The variational phase field bending elasticity model described in the previous section is conveniently stated as:

$$\begin{cases} \arg\min\limits_{\phi} E(\phi) = \displaystyle\int_\Omega \frac{k\epsilon}{2}\left[\triangle\phi - \frac{1}{\epsilon^2}(\phi^2-1)\phi\right]^2 dx, \\ A(\phi) = \displaystyle\int_\Omega \phi dx = \alpha, \\ B(\phi) = \displaystyle\int_\Omega \left[\frac{\epsilon}{2}|\nabla\phi|^2 + \frac{1}{4\epsilon}(\phi^2-1)^2\right]dx = \beta, \\ \phi|_{\partial\Omega} = 1, \end{cases} \tag{3.1}$$

where α and β are given constants, and $\Omega = [-1,1]^3$. The well-posedness of the above problem can be found in [19, 25]. The consistency to the original bending elasticity model when $\epsilon \to 0$ has also been examined in [19, 51].

To deal with the nonlinear constraints, a penalty formulation can be used. Let

$$G(\phi) = E(\phi) + M_1[A(\phi) - \alpha]^2 + M_2[B(\phi) - \beta]^2,$$

where M_1 and M_2 are penalty constants, and let us introduce

$$\lambda_M(\phi) = 2M_1[A(\phi) - \alpha] , \qquad \mu_M(\phi) = 2M_2[B(\phi) - \beta] .$$

As the penalty constants M_1 and M_2 go to infinity, the minimizer of G goes to the solution of the constrained problem, and λ_M and μ_M converge to the Lagrange multipliers [22, 25]. For the sake of simplicity, we denote them by λ and μ in the analysis. In the simulations, M_1 and M_2 are taken to be fixed large numbers that assure the convergence of the Lagrange multipliers to within the given numerical accuracy.

To derive the mixed weak formulation [26], we introduce a function f as

$$f = \sqrt{k\epsilon}\left[\triangle\phi - \frac{1}{\epsilon^2}(\phi^2 - 1)\phi\right] .$$

We note that f is a scaled phase field approximation of the mean curvature, and for small ϵ other boundary conditions such as the homogeneous Neumann boundary condition on ϕ may also be used.

Multiplying the equation for f by a test function $w \in H_0^1(\Omega)$ and integrating over Ω, after integration by parts, we get

$$\int_\Omega f w dx = -\sqrt{k\epsilon}\int_\Omega \left[\nabla\phi\cdot\nabla w + \frac{1}{\epsilon^2}(\phi^2 - 1)\phi w\right] dx$$

for any $w \in H_0^1(\Omega)$. Note that the boundary condition $\phi = 1$ is imposed.

Taking the variational derivative of the energy functional, we get

$$-\sqrt{k\epsilon}\int_\Omega \left[\nabla f\cdot\nabla v + \frac{1}{\epsilon^2}f(3\phi^2 - 1)v\right] dx + \int_\Omega \left(\lambda - \mu\sqrt{\frac{\epsilon}{k}}f\right) v dx = 0$$

for any $v \in H^1(\Omega)$. Given any spatial region $D \subseteq \Omega$, let

$$(u,v)_D = \int_D uv dx, \quad \|u\|_D = (u,u)_D^{1/2}$$

denote the standard L^2 inner product and the L^2 norm on D, respectively, and

$$\langle\nabla u, \nabla v\rangle_D = \int_D \nabla u\cdot\nabla v dx .$$

Let us define

$$\mathcal{H} = H^1(\Omega) \times H^1(\Omega) \quad \text{and} \quad \mathcal{H}_0 = H^1(\Omega) \times H_0^1(\Omega).$$

The weak form of our problem (3.1) is to find (f, ϕ) with $(f, \phi - 1) \in \mathcal{H}_0$ such that, for all $(v, w) \in \mathcal{H}_0$, we have

$$\begin{cases} -\sqrt{k\epsilon}\left[\langle \nabla f, \nabla v\rangle_\Omega + \frac{1}{\epsilon^2}\left(f(3\phi^2 - 1), v\right)_\Omega\right] + \lambda(1, v)_\Omega \\ \qquad -\mu\sqrt{\frac{\epsilon}{k}}(f, v)_\Omega = 0, \\ \sqrt{k\epsilon}\left[\langle \nabla \phi, \nabla w\rangle_\Omega + \frac{1}{\epsilon^2}\left((\phi^2 - 1)\phi, w\right)_\Omega\right] + (f, w)_\Omega = 0\ . \end{cases} \tag{3.2}$$

The above weak form leads naturally to a mixed FEM for its numerical solution [26].

Define the operator $F : \mathcal{H} \to \mathcal{L}(\mathcal{H}_0, R^2)$ by

$$\begin{aligned} &F(f, \phi)(v, w) \\ &\quad = \left(-\sqrt{k\epsilon}\left[\langle \nabla f, \nabla v\rangle_\Omega + \frac{1}{\epsilon^2}\left(f(3\phi^2 - 1), v\right)_\Omega\right]\right. \\ &\qquad\qquad +\lambda(1, v)_\Omega - \mu\sqrt{\frac{\epsilon}{k}}(f, v)_\Omega, \\ &\qquad \left. W\left[\sqrt{k\epsilon}\left(\langle \nabla \phi, \nabla w\rangle_\Omega + \frac{1}{\epsilon^2}\left((\phi^2 - 1)\phi, w\right)_\Omega\right) + (f, w)_\Omega\right]\right)^T, \end{aligned}$$

where W is a weight constant to be determined in simulations. Now the problem becomes that of solving

$$F(f, \phi) = 0 \tag{3.3}$$

in an abstract form, together with the boundary conditions.

To construct the finite element approximation to the mixed formulation, we take the discrete function space as

$$V_h = W_h = \{v \in C^0(\Omega) \cap H^1(\Omega) \ \mid\ v|_K \in P_1(K) \ \ \forall K \in J_h\},$$

where J_h is a triangulation of $\overline{\Omega}$ consisting of tetrahedra K, whose diameters h_K are bounded above by $h = \max_{K \in J_h} h_K$, and $P_1(K)$ denotes the linear function space on element K. The mesh is assumed to be regular so that the standard minimum angle condition is satisfied and the number of adjacent elements to any given element is bounded independently of h. We also assume that the family J_h is uniformly regular so that for any $K \in J_h$ the ratio of the diameter of K and the diameter of the largest ball enclosed in K is uniformly bounded from above by a constant independent of h. The detailed adaptive construction of J_h will be described later in the paper. Now, let

$$X_h = V_h \times W_h \quad \text{and} \quad X_h^0 = V_h^0 \times W_h,$$

where

$$V_h^0 = W_h^0 = \{v \mid v \in V_h, \ \ v|_{\partial\Omega} = 0\}.$$

For the trial solution $(f_h, \phi_h - 1) \in X_h^0$ satisfying the boundary conditions and the test function $(v_h, w_h) \in X_h^0$, we define the discrete version of F:

$$F_h(f_h, \phi_h)(v_h, w_h) = F(f_h, \phi_h)(v_h, w_h).$$

Hence the discrete problem is to solve

$$F_h(f_h, \phi_h) = 0. \tag{3.4}$$

The solutions of (3.3) and (3.4) depend on the parameters α and β. By normalization, we may always take $\beta = 1$(some constant surface area); then the solution of (3.3) may be viewed as a solution branch of

$$F(\alpha; x) = 0.$$

The basic mathematical analysis of the discretized system (such as the existence of solutions and an a priori error estimate, specialized to a piecewise linear element) has been made in [26]. In particular, if there exists a C^1 branch $\{\alpha, x(\alpha)\}$ of nonsingular solutions of the nonlinear variational problem (3.3) for $\alpha \in \Lambda$ which is a compact interval in R, then for small h there is a unique branch $\{\alpha, x_h(\alpha)\}$ of solutions of (3.4) converging to $\{\alpha, x(\alpha)\}$. Moreover, if $\alpha \to x(\alpha)$ is a C^1 function from Λ into $\mathcal{H} \cap (H^2(\Omega) \times H^2(\Omega))$, we have the optimal order a priori error estimate

$$\|x(\alpha) - x_h(\alpha)\|_{\mathcal{H}} \le Ch,$$

where C is a constant independent of h.

While the a priori error analysis can offer theoretical assurance on the convergence of the finite element methods as the mesh size gets smaller and smaller, to implement an adaptive strategy for the finite element approximations, we need a posteriori error estimators. We choose to work with residual-type estimators which are derived in the next section.

4. A posteriori error estimate. Adaptive methods often lead to efficient discretization to problems with solutions that are singular or have large variations in small scales. In phase field models, the sharp interface of physical quantities is replaced by regularized phase field functions. However, for a small interfacial width constant ϵ, the phase field solutions may display large gradients within the diffusive interfacial region. Thus, adaptivity in the form of mesh refinement and coarsening as well as mesh transformation can greatly improve the efficiency of the numerical approximations of phase field models [10, 27, 37, 44]. A posteriori error estimators are key ingredients in the design of adaptive methods [3]. There have been many existing studies on deriving such estimators for the finite element approximation of linear and nonlinear variational problems and for standard Galerkin and mixed finite element formulations; see, for example, [1, 8, 45, 50], and the references cited therein.

Let $x_0 = (f_0, \phi_0)$ be a solution of a nonlinear operator equation $F(x_0) = 0$. We call x_0 a regular solution if the Frechet derivative $DF(x_0)$ is well defined and is a linear homeomorphism; that is, $DF(x_0)$ and its inverse are bijective and continuous linear operators. First, using the abstract approximation results from [50] (see also

[7], and particular applications to Ginzburg–Landau-type models [16], and the phase field bending elasticity model of vesicle membranes presented in [26]), we immediately get the following.

PROPOSITION 4.1 (see [50]). *Let $\mathcal{H}_0^* = \mathcal{L}(\mathcal{H}_0, R^2)$ and $F \in C^1(\mathcal{H}, \mathcal{H}_0^*)$. Let x_0 be a regular solution of $F(x) = 0$ with $Z = ||DF(x_0)||_{\mathcal{L}(\mathcal{H}_0, \mathcal{H}_0^*)}$ and $\hat{Z} = ||DF(x_0)^{-1}||_{\mathcal{L}(\mathcal{H}_0^*, \mathcal{H}_0)}$. Assume, in addition, that DF is Lipschitz continuous at x_0 with a constant $\gamma > 0$, i.e., there is a M_0 such that*

$$\gamma := \sup_{||x - x_0||_{\mathcal{H}} < M_0} \frac{||DF(x) - DF(x_0)||_{\mathcal{L}(\mathcal{H}_0, \mathcal{H}_0^*)}}{||x - x_0||_{\mathcal{H}}} < \infty.$$

Set

$$M := \min\{M_0, \gamma^{-1}\hat{Z}^{-1}, 2\gamma^{-1}Z\}.$$

Then, for all $x \in \mathcal{H}$ with $||x - x_0||_{\mathcal{H}} < M$.

$$\frac{1}{2Z}||F(x)||_{\mathcal{H}_0^*} \le ||x - x_0||_{\mathcal{H}} \le 2\hat{Z}||F(x)||_{\mathcal{H}_0^*}. \tag{4.1}$$

To apply the above framework to our problem, one relevant issue is how the various constants γ, Z, $\hat{Z}$, and M depend on ϵ. We note that obtaining a very precise dependence in general is very difficult, and it remains largely as an open problem due to the nonlinear nature of the problem (see [29, 39, 42] for related discussion). Some crude estimates can be obtained, for example, by noticing that for given f_0, ϕ_0 the components of the vector-valued operator $DF(f_0, \phi_0)$ contain typical terms like $-\sqrt{k\epsilon}(\Delta + \frac{1}{\epsilon^2}(3\phi_0^2 - 1)I)$. It is then reasonable to take a typical tanh profile for ϕ_0 based on the earlier sharp interface limit analysis in [19] and to get estimates on the spectra of such operators. Similarly, one can estimate the Lipschitz constant γ. These estimates, however, are not sharp in general, and future studies are obviously needed to examine such dependence more carefully.

We now continue to derive a posteriori error estimators. Let $x_h = (f_h, \phi_h)$ be a solution of $F_h(x_h) = 0$ and R_h be a restriction or projection operator from $\mathcal{H}$ to the finite element space. For $y \in \mathcal{H}_0$, by Galerkin orthogonality

$$F_h(x_h)R_h y = 0.$$

Hence

$$F(x_h)y = F_h(x_h)y = F(x_h)(y - R_h y).$$

Specifically, let $R_h = [I_h, I_h]$, where I_h denotes the Clement interpolation [13]. We first note that, for a given element K and a given edge e defined by the triangulation J_h, the operator I_h has the following properties:

$$||u - I_h u||_K \le Ch_K||\nabla u||_{N(K)}$$

and

$$||u - I_h u||_{L^2(e)} \le Ch_e^{\frac{1}{2}}||\nabla u||_{N(e)},$$

where $N(K)$ denotes the union of K and its neighbor elements and $N(e)$ denotes the union of elements that have e as a face.

Next, we have

$$
\begin{aligned}
&||F(f_h,\phi_h)(v,w)|| = ||F(f_h,\phi_h)(v-I_hv, w-I_hw)||\\
&= \Bigg\{ \Bigg[-\sqrt{k\epsilon}\sum_K \langle \nabla f_h, \nabla(v-I_hv)\rangle_K \\
&\qquad + \sum_K \left(\left[\frac{-\sqrt{k}}{\epsilon^{3/2}} f_h(3\phi_h^2-1) + \lambda - \mu\sqrt{\frac{\epsilon}{k}} f_h \right], v-I_hv \right)_K \Bigg]^2 \\
&\quad + W^2 \Bigg[\sqrt{k\epsilon}\sum_K \langle \nabla\phi_h, \nabla(w-I_hw)\rangle_K \\
&\qquad + \sum_K \left(\left[f + \frac{\sqrt{k}}{\epsilon^{3/2}}(\phi_h^2-1)\phi_h \right], w-I_hw \right)_K \Bigg]^2 \Bigg\}^{\frac{1}{2}} \\
&\le C \Bigg\{ \Bigg[\sqrt{k\epsilon}\sum_{e\subset\Omega} h_e^{\frac{1}{2}} |e|^{\frac{1}{2}} \left| \left[\frac{\partial f_h}{\partial n} \right]_e \right| ||\nabla v||_{N(e)} \\
&\qquad + \sum_K h_K \left\| \lambda - \frac{\sqrt{k}}{\epsilon^{3/2}} f_h(3\phi_h^2-1) - \mu\sqrt{\frac{\epsilon}{k}} f_h \right\|_K ||\nabla v||_{N(K)} \Bigg]^2 \\
&\quad + W^2 \Bigg[\sqrt{k\epsilon}\sum_{e\subset\Omega} h_e^{\frac{1}{2}} |e|^{\frac{1}{2}} \left| \left[\frac{\partial \phi_h}{\partial n} \right]_e \right| ||\nabla w||_{N(e)} \\
&\qquad + \sum_K h_K \left\| f_h + \frac{\sqrt{k}}{\epsilon^{3/2}}(\phi_h^2-1)\phi_h \right\|_K ||\nabla w||_{N(K)} \Bigg]^2 \Bigg\}^{\frac{1}{2}}.
\end{aligned}
$$

Let

$$
\begin{aligned}
\eta_K = &\Bigg\{ \Bigg[C_1\sqrt{k\epsilon} \sum_{e\subset\Omega\cap\overline{K}} h_e^{\frac{1}{2}} |e|^{\frac{1}{2}} \left| \left[\frac{\partial f_h}{\partial n} \right]_e \right| + h_K \left\| \lambda - \frac{\sqrt{k}}{\epsilon^{3/2}} f_h(3\phi_h^2-1) - \mu\sqrt{\frac{\epsilon}{k}} f_h \right\|_K \Bigg]^2 \\
&+ W^2 \Bigg[C_2\sqrt{k\epsilon} \sum_{e\subset\Omega\cap\overline{K}} h_e^{\frac{1}{2}} |e|^{\frac{1}{2}} \left| \left[\frac{\partial \phi_h}{\partial n} \right]_e \right| + C_3 h_K \left\| f_h + \frac{\sqrt{k}}{\epsilon^{3/2}}(\phi_h^2-1)\phi_h \right\|_K \Bigg]^2 \Bigg\}^{\frac{1}{2}},
\end{aligned} \tag{4.2}
$$

where C_1, C_2, and C_3 are weights depending on constants in the interpolation inequalities. Without loss of generality, we simply take them to be 1, and the choice of the weight W used in the simulations is described later. We have

$$
\|F(f_h,\phi_h)\|_{\mathcal{L}(\mathcal{H}_0,R^2)} \le C \left\{ \sum_K \eta_K^2 \right\}^{\frac{1}{2}}.
$$

Applying Proposition 4.1, we get

$$
\|(f_h,\phi_h) - (f_0,\phi_0)\|_{\mathcal{H}} \le C \left\{ \sum_K \eta_K^2 \right\}^{\frac{1}{2}}. \tag{4.3}
$$

We would like to point out that the constant C depends on ϵ through $\hat{Z}$.

Let us now derive the following estimate.

LEMMA 4.1. *Let η_K be defined as in* (4.2) *and* (f_h, ϕ_h) *be a solution of* $F_h(f_h, \phi_h) = 0$. *Then*

$$\left\{\sum_K \eta_K^2\right\}^{\frac{1}{2}} \leq C_\epsilon ||F(f_h, \phi_h)||_{\mathcal{L}(\mathcal{H}_0, R^2)}.$$

Proof. Let $x_h = (f_h, \phi_h)$ denote a solution to the discrete problem, and let F_1 and F_2 denote the components of F, that is,

$$F(f, \phi)(v, w) = (F_1(f, \phi)v, F_2(f, \phi)w)^T.$$

Let

$$g = \lambda(\phi_h) - \frac{\sqrt{k}}{\epsilon^{3/2}} f_h(3\phi_h^2 - 1) - \mu(\phi_h)\sqrt{\frac{\epsilon}{k}} f_h.$$

For an element K, let v_K denote the element-bubble function given by

$$v_K = 256\psi_1\psi_2\psi_3\psi_4,$$

where $\{\psi_i\}_1^4$ are the nodal basis functions on K. Since g is a polynomial of degree 3 in K,

$$||g||_K^2 \leq C \int_K g^2 v_K dK = C F_1(x_h)(g v_K). \tag{4.4}$$

Notice that gv_K is a polynomial of degree 7 and v_K has maximum value 1, so we have

$$||g v_K||_{H^1(K)} \leq C h_K^{-1} ||g||_K. \tag{4.5}$$

Multiplying (4.4) and (4.5), we get

$$h_K ||g||_K \leq C ||g v_k||_{H^1(K)}^{-1} F_1(x_h)(g v_K). \tag{4.6}$$

For an internal face $e = K \cap K'$, let

$$g_e = \left| \left[\frac{\partial f_h}{\partial n} \right]_e \right|,$$

and denote the face-bubble function by

$$v_e = 27\psi_1\psi_2\psi_3,$$

where $\{\psi_i\}_1^3$ are the nodal basis functions of K corresponding to the 3 nodes on the face e; then

$$F_1(x_h)(g_e v_e) = -\sqrt{k\epsilon} \int_{K \cup K'} \nabla f_h \cdot g_e \nabla v_e dx + \int_{K \cup K'} g g_e v_e dx\ .$$

Hence,

$$\sqrt{k\epsilon} g_e^2 ||v_e||_{L^1(e)} \leq g_e |F_1(x_h)(v_e)| + g_e ||g||_K ||v_e||_K + g_e ||g||_{K'} ||v_e||_{K'}\ .$$

Let $|e|$ be the area of e. The face-bubble function v_e has the following properties:

$$\begin{aligned}
&||v_e||_{L^1(e)} \sim |e|,\\
&||v_e||_K \le C(h_K|e|)^{\frac{1}{2}},\\
&||v_e||_{H^1(K)} \le Ch_K^{-\frac{1}{2}}|e|^{\frac{1}{2}}.
\end{aligned}$$

Notice that $F_1(f,\phi)(\cdot)$ is a linear operator; we can choose the sign of v_e such that $|F_1(x_h)v_e| = F_1(x_h)v_e$. Together with (4.6) and the fact that the size of adjacent elements does not change rapidly, these give us

$$\begin{aligned}
\sqrt{k\epsilon}h_K^{\frac{1}{2}}|e|^{\frac{1}{2}}\left|\left[\frac{\partial f_h}{\partial n}\right]_e\right| \le C\Big\{&||v_e||_{H^1(K)}^{-1}F_1(x_h)(v_e)\\
&+||gv_K||_{H^1(K)}^{-1}F_1(x_h)(gv_K)\\
&+||gv_{K'}||_{H^1(K')}^{-1}F_1(x_h)(gv_{K'})\Big\}\ .
\end{aligned}$$

Let

$$u_e = \frac{v_e}{||v_e||_{H^1(K)}} + \frac{gv_K}{||gv_K||_{H^1(K)}} + \frac{gv_{K'}}{||gv_{K'}||_{H^1(K')}}.$$

We have

$$\sqrt{k\epsilon}h_K^{\frac{1}{2}}|e|^{\frac{1}{2}}\left|\left[\frac{\partial f_h}{\partial n}\right]_e\right| \le CF_1(x_h)u_e.$$

Estimation of the other two terms of η_K can be obtained similarly. Hence for every element K, we can find $y_K = (u_K, w_K) \in \mathcal{H}_0$ such that

$$0 \le \eta_K \le C(F_1(x_h)u_K + F_2(x_h)w_K), \quad ||y_K||_{\mathcal{H}_0} = 1, \quad \text{and} \quad \operatorname{supp}(u_K, w_K) \subset N(K)\ .$$

Let

$$a_K = \frac{\eta_K}{\sqrt{\sum_K \eta_K^2}}, \qquad y = (u,w) = \sum_K a_K y_K.$$

Then

$$\begin{aligned}
\left\{\sum_K \eta_K^2\right\}^{\frac{1}{2}} &= \sum_K a_K\eta_K\\
&\le C(F_1(x_h)u + F_2(x_h)w)\\
&\le C||y||_{\mathcal{H}_0}||F(x_h)||_{\mathcal{L}(\mathcal{H}_0,R^2)}.
\end{aligned}$$

Since the support of y_K's only overlaps with that of the adjacent ones, we get

$$||y||_{\mathcal{H}_0} \le C\left(\sum_K a_K^2||y_K||_{\mathcal{H}_0}^2\right)^{\frac{1}{2}} = C.$$

This completes the proof of Lemma 4.1. ∎

Combining Proposition 4.1 and Lemma 4.1, we get the following theorem.

THEOREM 4.1. *Let $\mathcal{H}_0^* = \mathcal{L}(\mathcal{H}_0, R^2)$ and $F \in C^1(\mathcal{H}, \mathcal{H}_0^*)$. Let x_0 be a regular solution of $F(x) = 0$ with $Z = ||DF(x_0)||_{\mathcal{L}(\mathcal{H}_0,\mathcal{H}_0^*)}$ and $\hat{Z} = ||DF(x_0)^{-1}||_{\mathcal{L}(\mathcal{H}_0^*,\mathcal{H}_0)}$. Assume, in addition, that DF is Lipschitz continuous at x_0 with a constant $\gamma > 0$, i.e., there is a M_0 such that*

$$\gamma := \sup_{||x-x_0||_{\mathcal{H}}<M_0} \frac{||DF(x) - DF(x_0)||_{\mathcal{L}(\mathcal{H}_0,\mathcal{H}_0^*)}}{||x - x_0||_{\mathcal{H}}} < \infty.$$

Set

$$M := \min\{M_0, \gamma^{-1}\hat{Z}^{-1}, 2\gamma^{-1}Z\}.$$

Let $x_h = (f_h, \phi_h)$ be the finite element solution to $F_h(x_h) = 0$. There exist positive constants M, C_{upper}, and C_{lower}, depending on γ and x_0, such that, when h is small enough and $||x_0 - x_h||_{\mathcal{H}} < M$, we have

$$C_{lower}\left\{\sum_K \eta_K^2\right\}^{\frac{1}{2}} \le ||x_0 - x_h||_{\mathcal{H}} \le C_{upper}\left\{\sum_K \eta_K^2\right\}^{\frac{1}{2}}, \tag{4.7}$$

where η_K's are defined as in (4.2).

The above theoretical analysis is used to guide us in the design of effective adaptive algorithms based on the a posteriori error estimator. A few comments are in order: as mentioned earlier, notice that the constants M, γ, C_{upper}, and C_{lower} depend on ϵ since the constants γ, $Z = ||DF(x_0)||$, and $\hat{Z} = ||DF(x_0)^{-1}||$ have such a dependence. Some of these constants rely on a priori information and may not be easily computable; we thus cannot completely assure the reliability and efficiency of the a posteriori error bounds theoretically, though such an issue is typical for many nonlinear variational problems [9] except in some limited cases [54]. Also, the condition $||x_h - x_0|| < M$ is satisfied only when h is small enough which may again, theoretically speaking, require a prohibitively small h, especially in comparison to ϵ. In addition, with possibly different constants for the lower and upper bounds in (4.7), the error estimator $\{\sum_K \eta_K^2\}^{\frac{1}{2}}$ may not be asymptotically exact in theory [50]. Nevertheless, our numerical experiments demonstrate that a very effective adaptive algorithm can be implemented for the phase field simulation based on the a posteriori error estimator $\{\sum_K \eta_K^2\}^{\frac{1}{2}}$ as defined by (4.2).

The details are to be described in the rest of the paper.

5. Adaptive algorithm. From a practical point of view the most interesting objects of the phase field models are related to a narrow transition region near the zero level set of the phase field function, which in our case provides information on the deformed membranes (as well as information on the interactions with external fields where they are present). It is thus easily concluded that some adaptive algorithms may lead to more efficient numerical schemes. We now discuss an adaptive FEM for the phase field bending elasticity model.

The common objective of an adaptive FEM is to generate a mesh which is adapted to the problem such that the error between the finite element solution and the exact solution is within the given error tolerance. Using $\{M_j\}_{j\ge 0}$ to represent the various level of meshes generated from the refinement and coarsening procedure, a description of the general adaptive algorithm is outlined below.

ALGORITHM 5.1. (ADAPTIVE FEM).
Start with mesh M_0 *and error tolerance tol*
set $j := 0; \eta := tol + 1$
while $\eta > tol$, *do*
solve the discrete problem on M_j
compute local error indicators η_K *and global error estimator* η
if $\eta > tol$
mark elements of M_j *for refinement or coarsening*
update M_j *to get* M_{j+1} *and set* $j := j + 1$
end if
end while.

Naturally, the objective of the marking strategy to be implemented in the above algorithm is to produce an efficient mesh. This is understood generally in the sense that one should provide more degrees of freedom where the error is big and less where the error is small. For linear elliptic problems, adaptive FEM often generates a quasi-optimal mesh with nearly equidistributed local errors, but, for nonlinear problems, the lack of resolution of the solution on coarse meshes may lead to some local refinement which is not needed for the final solution, and the mesh could be coarsened again. In the numerical implementation, we use the following marking strategy (where N denotes the number of elements of the current mesh and η is the total error).

ALGORITHM 5.2. (MARKING STRATEGY).
Start with given parameters $refine\_factor > 1$ *and* $coarsen\_factor < 1$
for all element K *do*
if $\eta_K > \frac{\eta}{\sqrt{N}} * refine\_factor$
mark K *for refinement*
end if
if $\eta_K < \frac{\eta}{\sqrt{N}} * coarsen\_factor$
mark K *for coarsening*
end if
end for.

In our simulations $refine\_factor = 1.4$ and $coarsen\_factor = 0.7$. We would like to mention that, during the mesh-updating procedure, elements marked for coarsening are actually coarsened only when the resulting mesh is still conforming. Since the variational problem considered here involves very complex nonlinearities, we next discuss some practical issues encountered in the implementation.

On a given mesh, the minimization of G is carried out using a gradient flow approach [22, 25]. Given ϕ_n and a step size Δt_n, the minimizer ϕ_{n+1} of

$$\frac{1}{2}\frac{||\phi_{n+1} - \phi_n||^2}{\Delta t_n} + G(\phi_{n+1}) \tag{5.1}$$

satisfies

$$\frac{\phi_{n+1} - \phi_n}{\Delta t_n} + \frac{\delta G}{\delta \phi}(\phi_{n+1}) = 0,$$

which is the backward Euler scheme of the gradient flow equation

$$\frac{\partial \phi}{\partial t} = -\frac{\delta G}{\delta \phi}.$$

Given an initial guess, as $t \to \infty$, the dynamic solutions $\{\phi(t)\}$ converge to a steady state which is a critical point of the energy G [4, 15, 35]. The solution of (5.1) at each

step is obtained using the nonlinear conjugate gradient (NCG) method. We adjust the time step Δt_n so that the NCG method converges in 8–15 steps. This allows efficient computation at each time step without the assembly of Hessian matrices. Several other nonlinear solvers can also be considered, such as the built-in Newton solver in *ALBERTA* [31], BFGS-type methods and augmented Lagrange multipliers [28], multigrid methods [30, 33], and other time-stepping schemes like the second order scheme in [25] and operator splitting schemes [4].

6. Numerical examples. We now present some numerical examples. Our objectives here are mainly to illustrate the effectiveness of the adaptive methods; thus, most of the computed vesicle shapes are ones which have also been computed by other methods as well [14, 22, 23, 28, 32, 41, 47, 53]. We let the computational domain be $[-1, 1]^3$ and for simplicity, let the elastic bending rigidity be $k = 1$. The mesh refinement and coarsening procedure is implemented with the help of the adaptive FEM toolbox *ALBERTA* [31].

In the experiments, the weight W in (4.2) is set to be $W = 100$. To illustrate how this weight is chosen, we first calculate the error estimators for a sphere using a tanh profile. That is, let $\phi = \tanh(\frac{|x|-R}{\sqrt{2}\epsilon})$, and start from its finite element approximation (interpolation) on a uniform initial mesh, we refine several times according to the error estimators and then calculate the percentage of the two terms in (4.2). We conduct several experiments with the radius $R = 0.8$, 0.5, 0.2 and $\epsilon = 0.03$, 0.02, 0.01, respectively. It is found that, when $W = 1$, the first term contributes to about 98% of the total error estimate for all nine cases. Thus, a choice of $W = 100$ leads to a balance of the two error components. Of course, the tanh function only gives a typical asymptotic profile [19] that provides us some hints on the possible scales of the terms in the error estimator. To validate this choice of weight W in our numerical simulations, a series of tests on numerical solutions are performed for $\epsilon = 0.048$ with W ranging from 0.01 to 10,000. The solution is taken to be an axis-symmetric disc, and the mesh density over the cross section $x_2 = 0$ is shown in Figure 6.1, from left to right, for $W = 0.01$, $W = 100$, and $W = 10,000$, respectively. The case of $W = 100$ tends to give a more reasonable mesh distribution. Moreover, the simulation results again show that the choice of $W = 100$ makes the corresponding two terms in the error estimator have comparable magnitude. It turns out that the same can be verified for the other simulations presented in this paper.

The transition width parameter ϵ is often assigned several different values in the range of 0.01 to 0.05 so that the results can be compared to ensure the fidelity of the phase field approximation to the sharp surface model [19, 23]. However, to save space,

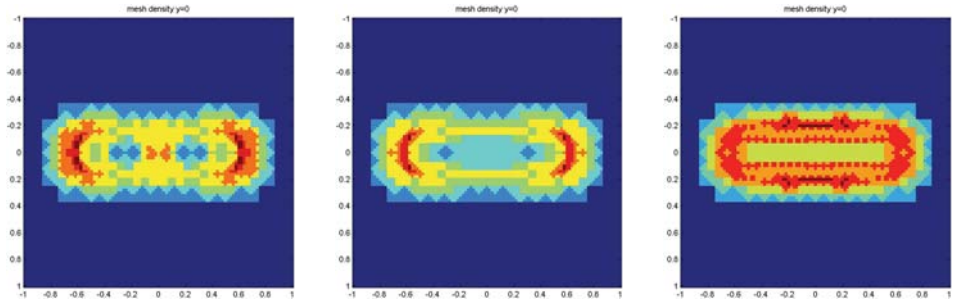

FIG. 6.1. *Mesh density on cross section* $x_2 = 0$ *for* $W = 0.01$, $W = 100$, *and* $W = 10{,}000$.

most of the results shown here are for the case of $\epsilon = 0.03$. Making further reduction in ϵ would not affect the results of the numerically simulated vesicle membrane shapes, although the level of adaptivity will certainly be influenced. Such dependence will be examined in more detail later, and the related analysis also serves to quantitatively measure the effectiveness of the adaptivity algorithm.

Simulating a solution branch with changing excess area. In the membrane simulation community, the excess area of a compact surface Γ is defined as the difference between its area and the area of the sphere having the same volume as that enclosed by Γ, motivated by the fact that the surface with minimum surface area with a given volume is necessarily a sphere. It is known that, for a range of the excess area, a continuous solution branch of energy-minimizing shapes exists, and it undergoes the deformation from a more elliptical shape to that of the discocytes (biconcave shape). We first used our adaptive algorithms to calculate such a solution branch.

Let us take a three-dimensional ellipsoid

$$\frac{x_1^2}{a^2} + \frac{x_2^2}{a^2} + \frac{(bx_3)^2}{a^2} = 1$$

as the initial membrane surface, which in general is not energy-minimizing. The initial value of the phase field function ϕ is assigned according to the formula

$$\phi_0(x) = \tanh\left(\frac{d(x)}{\sqrt{2}\epsilon}\right),$$

where $d(x)$ is the distance from $x = (x_1, x_2, x_3)$ to the membrane surface.

Since we are mostly interested in the shape of the energy-minimizing surface, the initial value of ϕ does not have to accurately fit the constraints nor have a good tanh profile. Thus, in our experiments, $d(x)$ is calculated approximately using

$$d(x) \sim \sqrt{x_1^2 + x_2^2 + (bx_3)^2} - a\ . \tag{6.1}$$

We let $a = 0.6$; the constraints on volume and surface area are chosen by setting $\alpha = A(\phi_0)$, and $\beta = B(\phi_0)$ for different values of b. Beginning with an uniform mesh with 17^3 nodes, we refine the mesh several times according to the error estimator calculated using ϕ_0 to get the initial mesh, so that α and β provide accurate values of the volume and surface area for the associated level surface.

We have also made various selections of the penalty constants M_1 and M_2. Based on the experiments, we find that it is adequate to choose the penalty constants $M_1 = 100$ and $M_2 = 10,000$, respectively. With this choice, the volume and surface area constraints are satisfied with less than 0.5% error, and the convergence of the Lagrange multipliers can also be observed.

Table 6.1 provides the numerical estimates to the constraints and the energy values corresponding to the minimizing shapes for different values of b. We can scale the volume of the membrane to be of unit volume since the bending energy is scale invariant. With such a scaling, the rescaled surface areas (denoted by $Area^1$) are calculated, and they are naturally linked to the so-called excess areas described earlier, so that for larger values of b, we have larger excess areas. The results of Table 6.1 illustrate quantitatively the dependence of the minimum energy with respect to the excess area.

In Figures 6.2–6.4, the energy-minimizing membrane shapes (obtained by the zero level sets of the phase field functions) are shown, along with some density plots of

TABLE 6.1
Values of volume, area, rescaled area, and energy.

b	α	β	Volume	Area	$Area^1$	Energy
1.6	6.8253	3.4548	0.5873	3.6644	5.23	30.27
1.8	6.9559	3.3367	0.5221	3.5391	5.46	33.79
2.0	7.0596	3.2840	0.4702	3.4832	5.76	38.19
2.2	7.1470	3.2399	0.4265	3.4364	6.06	42.34
2.4	7.2175	3.2333	0.3912	3.4294	6.41	45.96
2.6	7.2772	3.2663	0.3614	3.4644	6.83	51.27

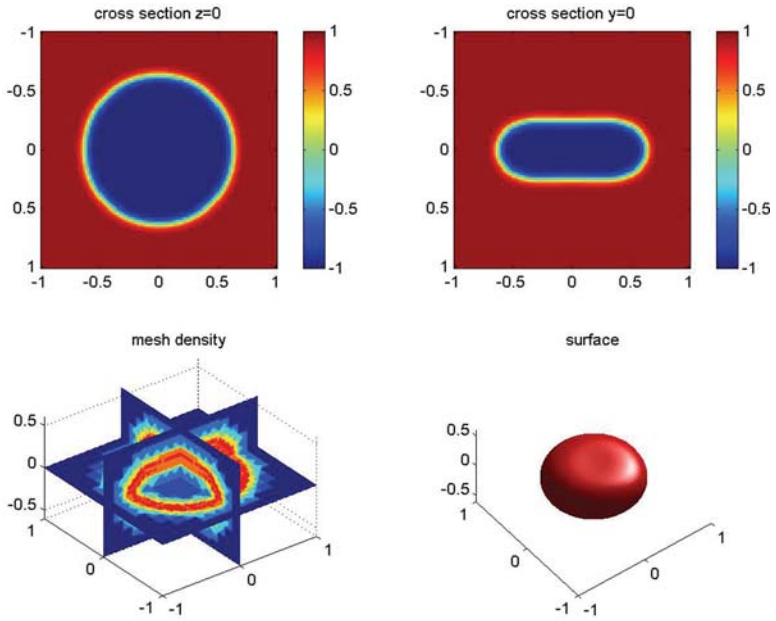

FIG. 6.2. *Solution and mesh density for* $b = 1.8$.

the cross sections of the phase field functions (the red color symbolizes $\phi = 1$ in the exterior of the membrane, while the blue color shows $\phi = -1$ inside the membrane). The three-dimensional sliced views of the densities of the corresponding adaptive meshes are provided (with the red color showing the most refined, or densely packed, meshing region and the blue color for the coarsest meshes; note the difference in the color coding for the solution profile and the mesh density distribution). The deformation to the discocytes for larger values of b is clearly seen from these figures. To get some ideas on what the actual phase field functions look like (not only their zero level set), Figure 6.5 shows the profile of ϕ and mesh density on cross sections $z = 0$ and $y = 0$ when $b = 2.6$. For a better view, the profiles of $-\phi$ are plotted instead. Figure 6.6 shows the profile of ϕ and mesh density for the same solution but with $\epsilon = 0.01$. It is clear that the profile is well resolved by the adaptive scheme.

We would like to comment on the dependence of the mesh on the curvature of the solution. First, on a heuristic ground, the membrane curvature should play a role in dictating the local mesh refinement, and the impact of the curvature with respect to the resolution of the phase field is affected by the choice of W, as we see in Figure 6.1. When $W = 100$, the magnitude of the two terms are comparable (in this case about 2:3 for both $\epsilon = 0.03$ and $\epsilon = 0.01$). In both Figures 6.5 and 6.6, the mesh

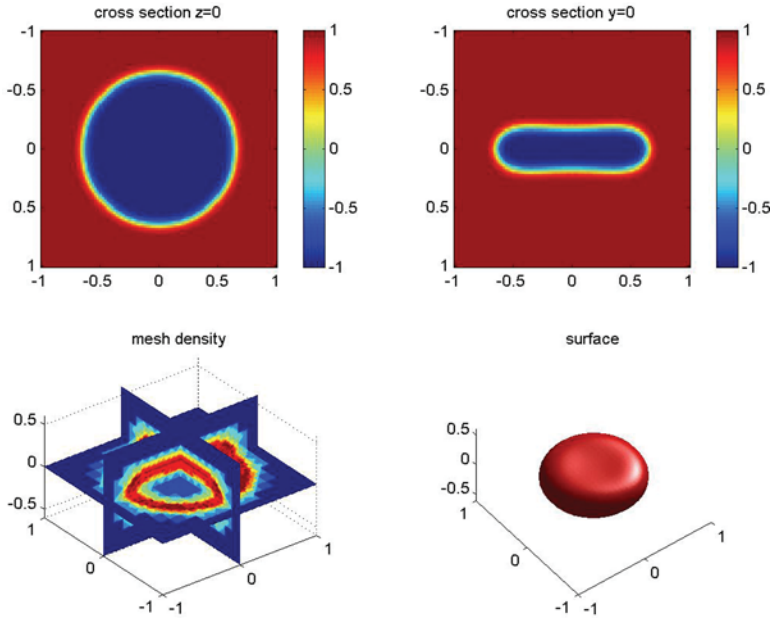

FIG. 6.3. *Solution and mesh density for* $b = 2.2$.

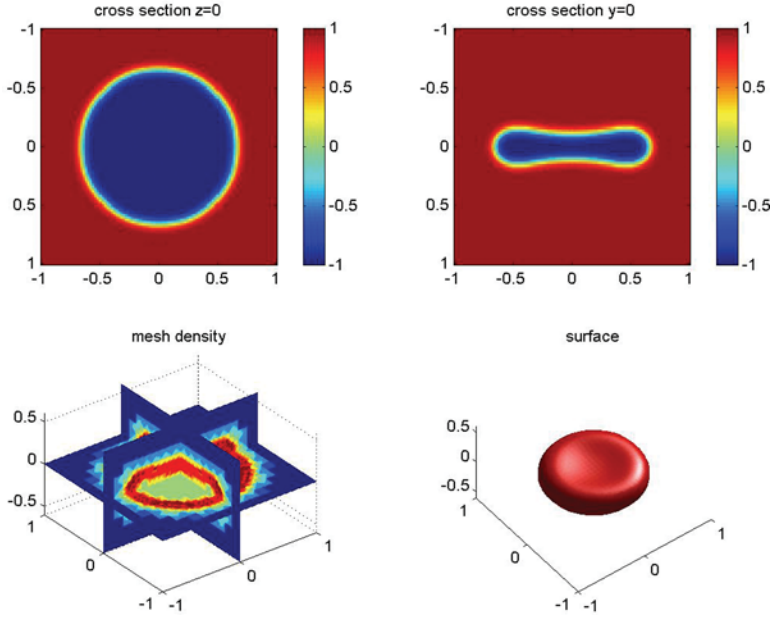

FIG. 6.4. *Solution and mesh density for* $b = 2.6$.

density at the two ends is a little higher than that in the middle. To get a better view of the local mesh refinement we zoomed in the upper left of the mesh density and plotted it in Figure 6.7. The effect of curvature can also be seen clearly in another simulation. Figure 6.8 shows a stomacytes-shaped energy-minimizing surface and the corresponding mesh density over a cross section where there is a bigger concentration of mesh points in the large curvature region near the axis.

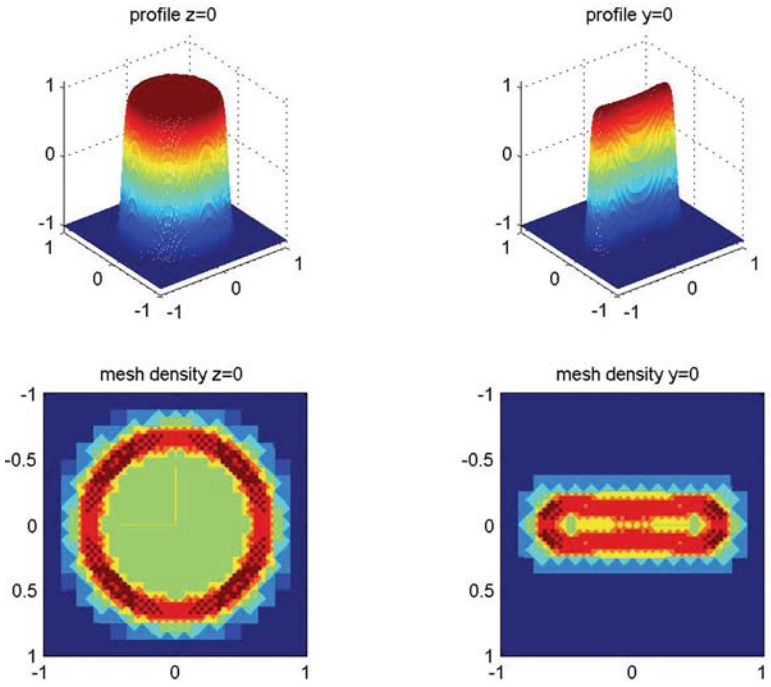

FIG. 6.5. *Profile and mesh of solution for* $b = 2.6$ *and* $\epsilon = 0.03$.

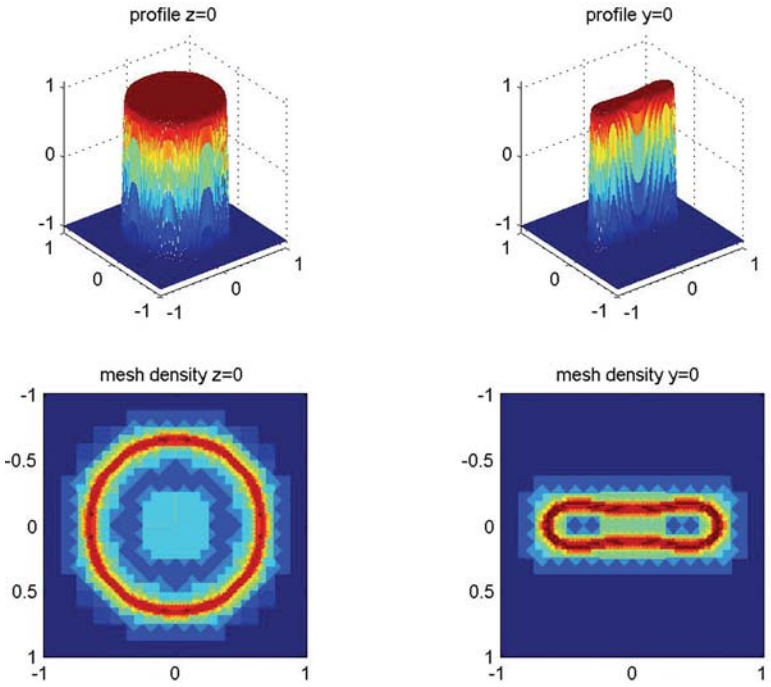

FIG. 6.6. *Profile and mesh of solution for* $b = 2.6$ *and* $\epsilon = 0.01$.

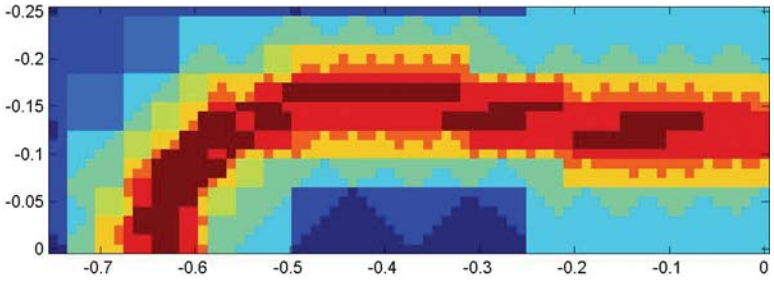

FIG. 6.7. *An enlarged view of the upper left part of the mesh density plot in Figure* 6.6.

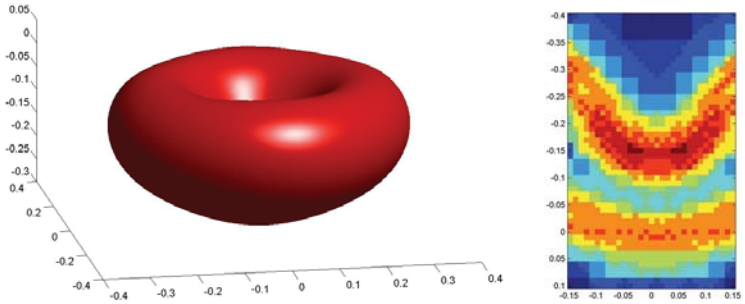

FIG. 6.8. *A stomacytes-shaped solution and the mesh density.*

TABLE 6.2
Number of nodes and estimated error.

Number of nodes (N)	45,166	63,113	81,603	112,425	140,007	302,107
Estimated error (E)	464.40	413.88	367.43	317.23	277.68	192.60

Quantitative measures for the efficiency of the adaptive scheme. In many simple contexts, the efficiency of the adaptive method is often illustrated by testing against a known exact solution, and the number of the total degrees of freedom used in the simulation against a certain error tolerance level are compared as a measure for the effectiveness of adaptivity. For our problem, however, the exact solutions in general are not easy to obtain.

We designed two series of simulations to address this issue.

First, we take the solution shown in Figure 6.8, fix ϵ, and solve for the same energy-minimizing surface using more and more nodes. Instead of studying the relation between the error and the mesh size, we studied the relation between the total number of nodes and the error for the reason that the sizes of the elements vary in an adaptive mesh. Table 6.2 shows the number of nodes and the estimated errors.

We speculate that, for the estimated error E, a relation to the number of nodes like

$$\log(E) \sim C + \delta \log(N)$$

may be expected. A linear regression can then be used to estimate C and δ. The estimated error and the fitted line are shown in Figure 6.9.

This result shows that the estimated error is on the order of $N^{-0.4723}$, which is close to the $N^{-1/2}$ as projected by theory: since we are using isotropic elements,

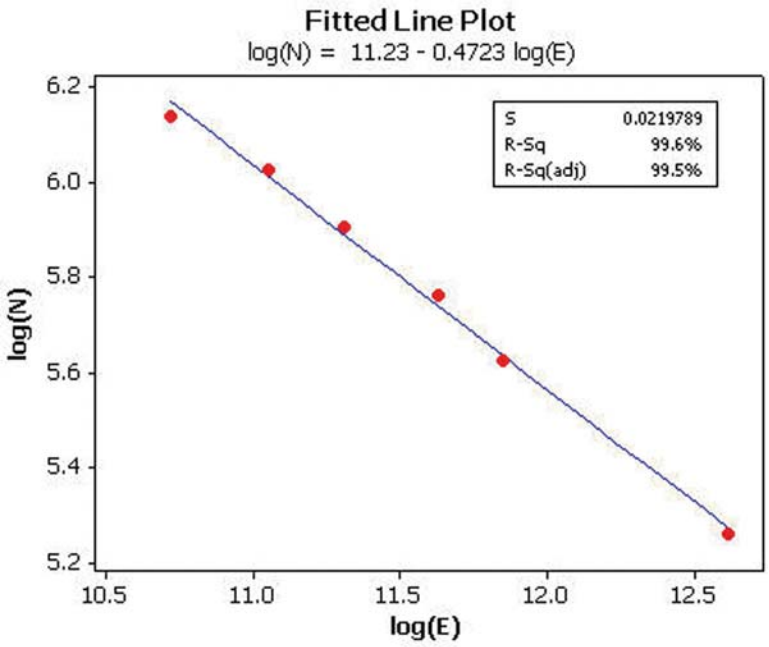

FIG. 6.9. *Number of nodes vs. estimated error.*

TABLE 6.3
Number of nodes and norms of the differences in solutions.

Number of nodes (N)	45,166	63,113	81,603	112,425	140,007
H^1 norm of $f_i - f_0$	481.0800	399.4072	338.0796	265.6828	217.7660
H^1 norm of $\phi_i - \phi_0$	5.7128	4.3948	3.4876	2.7824	2.3988

an almost uniformly structured fine mesh may be expected near the membrane; in this case we should expect the estimated error to be on the order of $N^{-1/2}$ so that the complexity of the three-dimensional (3D) adaptive FEM is comparable with a 2D uniform mesh. Of course, in the numerical simulations, as shown earlier, the curvature of the membrane still plays a role in dictating the mesh refinement, so that the adaptive mesh in general does not always have the same structure over the whole membrane, thus leading to small variations to the projected order.

Next, the relation between the actual H^1 error and N is provided. The difficulty in getting such a relation is that the actual H_1 error is unknown since no exact solution is available. We first decide to use the solution on the finest mesh as an approximation to the exact solution and compute the differences of the other solutions with it. Table 6.3 shows the H^1 norm of the differences.

In Table 6.3, f_0 and ϕ_0 denote the solution of the mesh with 302,107 nodes. Since the error of the solution at the finest level cannot really be ignored, we check to see if asymptotically we have the following dependence:

$$||f_i - f_0||_{H^1} + ||\phi_i - \phi_0||_{H^1} \sim \left(\frac{1}{N_i} - \frac{1}{N_0}\right)^{1/2}, \tag{6.2}$$

where $N_0 = 302{,}107$ is the number of nodes of the finest mesh. The ratios of the left-

TABLE 6.4
Ratios between left-hand side and right-hand side in (6.2).

Number of nodes (N)	45,166	63,113	81,603	112,425	140,007
ratio / 10^5	1.1218	1.1406	1.1421	1.1360	1.1246

hand side and the right-hand side of (6.2) are shown in Table 6.4, which indicates that (6.2) is a good match of the simulation results with the predicted behavior. Notice that, if we take N_0 to infinity so that (f_0, ϕ_0) approaches the exact solution, we then get an asymptotic convergence of the H^1 error like $\sim N^{-1/2}$ as demonstrated for the estimated error.

Combining the above discussions of the estimated error and the differences between numerical solutions, we see that for a given interfacial width parameter, as we increase the level of numerical resolution, the a posteriori error estimators provided good predictions of the quantitative behavior of the actual numerical error.

To demonstrate the efficiency of adaptive methods more quantitatively as ϵ gets smaller and smaller, we borrow ideas from the asymptotic sharp interface limit of the phase field model. By the analysis in [19] and the simulations presented earlier in [22, 23], we see that a solution to the phase field model typically has a tanh profile and the width of the transition layer is proportional to ϵ for small ϵ. Suppose we would like to keep the same level of resolution within the transition layer; we expect the size of the elements near the transition layer to be on the order of ϵ (we refer to [29, 39, 42] for more detailed analysis on various numerical approximations of similar phase field models and the dependence of the mesh size on the interfacial width for quasi-uniform meshes). In such a case, if uniform meshes are used, the number of nodes would grow at a rate proportional to at least ϵ^{-3} in order to maintain asymptotically the same level of numerical resolution. For an isotropic adaptive mesh with nodes being concentrated near the transition layer, we naturally expect the number of nodes to be proportional to at least ϵ^{-2}. Based on the above observation, we conduct another series of tests to check the theoretical prediction. As the errors cannot be controlled exactly as desired, we scale the number of nodes according to the estimated error under the assumption that the estimated error of the solution is proportional to $N^{-1/2}$.

We now present the results of a series of ten simulations with different ϵ, for the case $b = 1.6$ and $b = 2.4$, respectively. Figure 6.10 shows the number of nodes needed in order to achieve the same accuracy (estimated error) for different values of ϵ. The blue "*" symbols are the experimental data, and the blue dashed line is the estimated number of nodes using the formula $N = C\epsilon^{-2}$ for the case $b = 1.6$, while the red "$\circ$" symbols are experimental data, and the red solid line is the estimated N corresponding to the case $b = 2.4$. The plots are in log-log scale, so that a negative slope of -2 (for the dashed and solid lines) is expected and the actual numerical data largely follow the same trend.

These simulation results support the theoretical prediction based on the asymptotic analysis and also serve as a quantitative measurement on the efficiency of the adaptive method.

High genus energy-minimizing vesicles. We also conducted experiments with other values of the parameters and obtained other solutions as shown in [22, 23]. Those results are omitted here. Instead, let us briefly describe a new simulation result computed with the adaptive method. Figure 6.11 shows the result of one experiment which followed the path of four merging spheres. The transition width parameter is taken to be $\epsilon = 0.04$, the volume is constrained to be the same as the initial value,

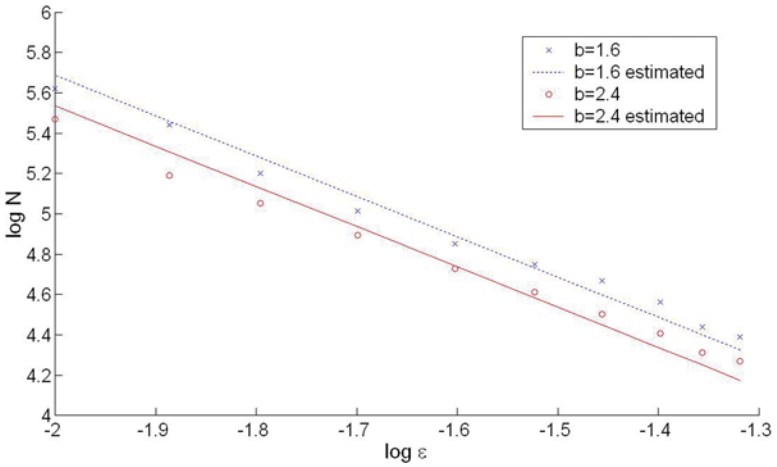

FIG. 6.10. *Number of nodes vs. the transition width parameter ϵ.*

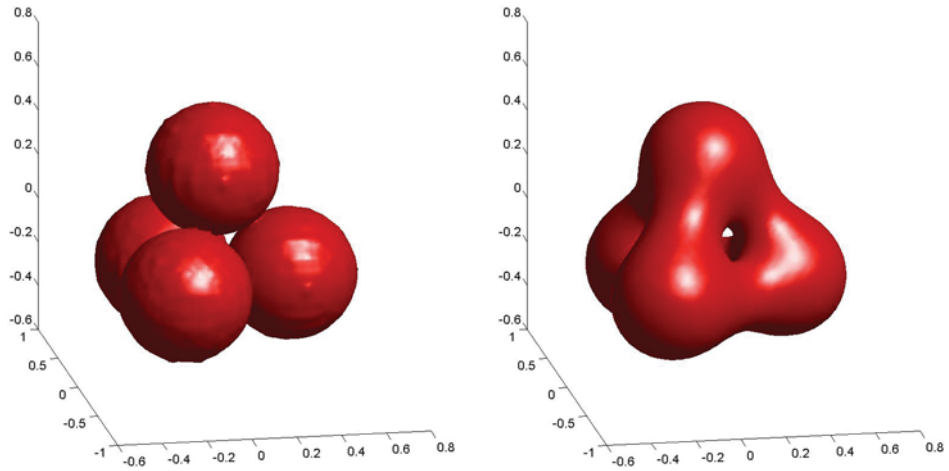

FIG. 6.11. *Initial surface and the energy minimizing surface with a smaller surface area.*

but the area is set to be 90% of the initial value. The initial profile showing the four small spheres appears to be less smooth, and this is due to the coarser meshes implemented in the beginning of the simulation. The reason to fix a slightly reduced surface area is to allow bigger perturbations to the initial profile and to allow the adaptive mesh to make self-adjustment based on the resolution need. As the deformation begins, meshes are adaptively refined and coarsened so that, in the end, there is very good resolution near the equilibrium membrane surface. Topological transformation takes place during the deformation as the spheres merge together. We note, however, that the change of topology may lead to contributions due to the Gaussian curvature energy whose effect has been ignored in the simulation reported here.

The simulated result not only gives evidence to the capability of the phase field method in handling naturally the topological changes in the membranes, but it again confirms the rich variety of the bending energy-minimizing membrane subject to the volume and surface area constraints. We refer to [41, 47] for more discussions on this type of non-axis-symmetric and high topological genus energy-minimizing surfaces.

The experimental findings reported in this section are mostly designed to provide evidence to the effectiveness of the adaptive FEM discussed in this paper. We leave other computational results and their biological relevance to be reported in future works.

7. Conclusion. The study of vesicle membrane deformation is receiving more and more attention due to its fundamental importance and its close connection with many biological functions. The variational phase field bending elasticity model of vesicle membrane deformations has been demonstrated as an effective approach to study the vesicle membrane deformations [22, 23]. The phase field model requires the simulation of the phase field function in a computational domain enclosing the vesicle membrane. Since the objects of central interest are the membranes themselves and the phase field function also undergoes more significant variations around the membrane surfaces, it is highly desirable to design adaptive numerical algorithms for the phase field bending elasticity model. The three-dimensional adaptive finite element method developed in this paper meets this need. In our adaptive method, the mesh adaptivity is based on a residual-type a posteriori error estimator which is rigorously derived for the associated nonlinear system of partial differential equations. The effectiveness of the method is demonstrated through numerical simulation examples presented here that include the simulations of known solution branches and new high genus vesicles as well as quantitative experimental investigation on the adaptivity efficiency. This constitutes another step forward in making the phased field modeling approach a valuable tool for biophysicists and biologists to study interesting problems related to lipid bilayer membranes.

The phase field bending elasticity models and simulation tools have the potential to be very helpful in the study of the geometry, mechanics, and function of complex lipid membrane systems. Recent extensions have been made to the study of multicomponent vesicles, vesicles with free edges [52], and membranes interacting with background fluid flows [5, 18]. The extension of the adaptive algorithms to more general cases and other types of error estimators as well as their applications in multiscale modeling of bilayer vesicles and other more biologically realistic membrane models are currently under investigation.

REFERENCES

[1] S. Adjerid, *A posteriori error estimates for fourth-order elliptic problems*, Comput. Methods Appl. Mech. Engrg., 191 (2002), pp. 2539–2559.
[2] M. Ainsworth and J.T. Oden, *A posteriori error estimation in finite element analysis*, Comput. Methods Appl. Mech. Engrg, 142 (1997), pp. 1–88.
[3] I. Babuska and T. Strouboulis, *The Finite Element Method and Its Reliability*, Oxford University Press, London, 2001.
[4] W. Bao and Q. Du, *Computing the ground state solution of Bose–Einstein condensates by a normalized gradient flow*, SIAM J. Sci. Comput., 25 (2004), pp. 1674–1697.
[5] T. Biben, K. Kassner, and C. Misbah, *Phase-field approach to 3D vesicle dynamics*, Phys. Rev. E, 72 (2005), pp. 419–421.
[6] M. Bloor and M. Wilson, *Method for efficient shape parameterization of fluid membranes and vesicles*, Phys. Rev. E, 61 (2000), pp. 4218–4229.
[7] F. Brezzi, J. Rappaz, and P. Raviart, *Finite dimensional approximation of nonlinear problems part* I: *Branches of nonsingular solutions*, Numer. Math., 36 (1980), pp. 1–25.
[8] C. Carstensen, *A posteriori error estimate for the mixed finite element method*, Math. Comp., 66 (1997), pp. 465–476.
[9] C. Carstensen and D. Praetorius, *Numerical analysis for a macroscopic model in micromagnetics*, SIAM J. Numer. Anal., 42 (2005), pp. 2633–2651.

[10] Z. Chen, R. Nochetto, and A. Schmidt, *Error control and adaptivity for a phase relaxation model*, M2AN Math. Model. Numer. Anal., 34 (2000), pp. 775–797.
[11] P.G. Ciarlet, *Introduction to Linear Shell Theory*, I, in Ser. Appl. Math., Gauthier–Villars, Paris, 1998.
[12] P.G. Ciarlet, *Mathematical Elasticity*, III, in Stud. Math. Appl. 29, North–Holland, Amsterdam, 2000.
[13] P. Clement, *Approximation by finite element functions using local regularization*, RAIRO Anal. Numer., 9 (1975), pp. 77–84.
[14] H. Döbereiner, E. Evans, M. Kraus, U. Seifert, and M. Wortis, *Mapping vesicle shapes into the phase diagram: A comparison of experiment and theory*, Phys. Rev. E, 55 (1997), pp. 4458–4474.
[15] Q. Du, *Finie element methods for the time dependent Ginzburg–Landau model of superconductivity*, Comput. Math. Appl., 27 (1994), pp. 119–133.
[16] Q. Du, M. Gunzburger, and J. Peterson, *Analysis and approximation of the Ginzburg–Landau model of superconductivity*, SIAM Rev., 34 (1992), pp. 54–81.
[17] Q. Du, M. Li, and C. Liu, *Analysis of a phase field Navier-Stokes vesicle-fluid interaction model*, Discrete Contin. Dyn. Syst. Ser. B, 8 (2007), pp. 539–556.
[18] Q. Du, C. Liu, R. Ryham, and X. Wang, *Energetic variational approaches to modeling vesicle and fluid interactions*, SIAM J. Appl. Math., submitted.
[19] Q. Du, C. Liu, R. Ryham, and X. Wang, *A phase field formulation of the Willmore problem*, Nonlinearity, 18 (2005), pp. 1249–1267.
[20] Q. Du, C. Liu, R. Ryham, and X. Wang, *Modeling the spontaneous curvature effects in static cell membrane deformations by a phase field formulation*, Commun. Pure Appl. Anal., 4 (2005), pp. 537–548.
[21] Q. Du, C. Liu, R. Ryham, and X. Wang, *Diffuse interface energies capturing the Euler number: Relaxation and renomalization*, Commun. Math. Sci., 5 (2007), pp. 233–242.
[22] Q. Du, C. Liu, and X. Wang, *A phase field approach in the numerical study of the elastic bending energy for vesical membranes*, J. Comput. Phys., 198 (2004), pp. 450–468.
[23] Q. Du, C. Liu, and X. Wang, *Simulating the deformation of vesicle membranes under elastic bending energy in three dimensions*, J. Comput. Phys., 212 (2005), pp. 757–777.
[24] Q. Du, C. Liu, and X. Wang, *Retrieving topological information for phase field models*, SIAM J. Appl. Math., 65 (2005), pp. 1913–1932.
[25] Q. Du and X. Wang, *Convergence of numerical approximations to a phase field bending elasticity model of membrane deformations*, Int. J. Numer. Anal. Model., 4 (2006), pp. 441–459.
[26] Q. Du and L. Zhu, *Analysis of a mixed finite element method for a phase field elastic bending energy model of vesicle membrane deformation*, J. Comput. Math., 24 (2006), pp. 265–280.
[27] W.M. Feng, P. Yu, S.Y. Hu, Z.K. Liu, Q. Du, and L.Q. Chen, *Spectral implementation of an adaptive moving mesh method for phase-field equations*, J. Comput. Phys., 220 (2006), pp. 498–510.
[28] F. Feng and W. Klug, *Finite element modeling of lipid bilayer membranes*, J. Comput. Phys., 20 (2006), pp. 394–408.
[29] X. Feng and A. Prohl, *Analysis of a fully discrete finite element method for the phase field model and approximation of its sharp interface limits*, Math. Comp., 73 (2004), pp. 541–567.
[30] R. Hoppe and R. Kornhuber, *Adaptive multilevel methods for obstacle problems*, SIAM J. Numer. Anal., 31 (1994), pp. 301–323.
[31] A. Schmidt and K. Siebert, *Design of Adaptive Finite Element Software: The Finite Element Toolbox ALBERTA*, Lect. Notes Comput. Sci. Engrg. 42, 2005, Springer, Berlin.
[32] M. Jaric, U. Seifert, W. Wintz, and M. Wortis, *Vesicular instabilities: The prolate-to-oblate transition and other shape instabilities of fluid bilayer membranes*, Phys. Rev. Lett., 52 (1995), 6623.
[33] J.S. Kim, K.K. Kang, and J.S. Lowengrub, *Conservative multigrid methods for Cahn-Hilliard fluids*, J. Comput. Phys., 193 (2004), pp. 511–543.
[34] R.J. Leveque and Z. Li, *Immersed Interface Methods for Stokes flow with elastic boundaries or surface tension*, SIAM J. Sci. Comput., 18 (1997), pp. 709–735.
[35] F.-H. Lin and Q. Du, *Ginzburg–Landau vortices, dynamics, pinning and hysteresis*, SIAM J. Math. Anal., 28 (1997), pp. 1265–1293.
[36] R. Lipowsky, *The conformation of membranes*, Nature, 349 (1991), pp. 475–481.
[37] J.A. Mackenzie and M.L. Robertson, *A moving mesh method for the solution of the one-dimensional phase-field equations*, J. Comput. Phys., 181 (2002), pp. 526–544.
[38] O. Mouritsen, *Life - As a Matter of Fat: The Emerging Science of Lipidomics*, Springer, Berlin, 2005.

[39] X. Jiang and R. Nochetto, *A $P^1 - P^1$ finite element method for a phase relaxation model* I: *Quasi-uniform mesh*, SIAM J. Numer. Anal., 35 (1998), pp. 1176–1190.
[40] S. Osher and J. A. Sethian, *Fronts propagating with curvature-dependent speed: Algorithms based on Hamilton-Jacobi formulations*, J. Comput. Phys., 79 (1988), pp. 12–49.
[41] Z. Ou-Yang, J. Liu, and Y. Xie, *Geometric Methods in the Elastic Theory of Membranes in Liquid Crystal Phases*, World Scientific, Singapore, 1999.
[42] M. Paolini and C. Verdi, *Asymptotic and numerical analyses of the mean curvature flow with a space-dependent relaxation parameter,* Asympto. Anal., 5 (1992), pp. 553–574.
[43] C. Pozrikidis, *Effect of membrane bending stiffness on the deformation of capsules in simple shear flow*, J. Fluid Mech., 440 (2001), pp. 269–291.
[44] N. Provatas, N. Goldenfeld, and J. Dantzig, *Efficient computation of dendritic microstructures using adaptive mesh refinement*, Phys. Rev. Lett., 80 (1998), pp. 3308–3311.
[45] S. Repin, *A posteriori error estimation for variational problems with uniformly convex functionals*, Math. Comp., 69 (1999), pp. 481–500.
[46] A. Roma, C. Peskin, and ,M. Berger, *An adaptive version of the immersed boundary method*, J. Comput. Phys., 153 (1999), pp. 509–534.
[47] U. Seifert, *Configurations of fluid membranes and vesicles*, Adv. Phys., 46 (1997), pp. 13–137.
[48] U. Seifert, K. Berndl, and R. Lipowsky, *Configurations of fluid membranes and vesicles*, Phys. Rev. A, 44 (1991), pp. 1182–1202.
[49] S. Sukumaran and U. Seifert, *Influence of shear flow on vesicles near a wall: A numerical study*, Phys. Rev. E, 64 (2001), pp. 1–11.
[50] R. Verfurth, *A Review of A Posteriori Error Estimation and Adaptive Mesh-Refinement Techniques*, Wiley and Teubner, Chichester and Stuttgart, 1996.
[51] X. Wang, *Asymptotic analysis of phase field formulations of bending elasticity models*, SIAM J. Math. Anal., 39 (2008), pp. 1367–1401.
[52] X. Wang and Q. Du, *Modelling and simulations of multi-component lipid membranes and open membranes via diffusive interface approaches*, J. Math. Biol., 56 (2007), pp. 347–371.
[53] W. Wintz, H. Döbereiner, and U. Seifert, *Starfish vesicles*, Europhys. Lett., 33 (1996), pp. 403–408.
[54] A. Veeser, *Efficient and reliable a posteriori error estimators for elliptic obstacle problems*, SIAM J. Numer. Anal., 39 (2001), pp. 146–167.